Proton-induced fission at 190 MeV of ^{nat}W, ^{197}Au, ^{nat}Pb, ^{208}Pb, and ^{232}Th

M. C. Duijvestijn and A. J. Koning
Netherlands Energy Research Foundation ECN, Westerduinweg 3, NL-1755 ZG, Petten, The Netherlands

J. P. M. Beijers, A. Ferrari, M. Gastal, J. van Klinken, and R. W. Ostendorf
Kernfysisch Versneller Instituut KVI, Zernikelaan 25, NL-9747 AA, Groningen, The Netherlands

(Received 27 August 1998)

Proton-induced fission at 190 MeV of ^{nat}W, ^{197}Au, ^{nat}Pb, ^{208}Pb, and ^{232}Th is studied by means of an innovative method based on activation analysis. The fission-product mass distribution is reconstructed from the fission-product yields, which are obtained from off-line observed γ-ray spectra. For ^{nat}W, ^{197}Au, ^{208}Pb, and ^{nat}Pb the fission process results in a symmetric mass distribution. In the case of ^{232}Th the mass yield curve is decomposed into a mixed symmetric-asymmetric contribution originating from fissioning nuclides in the neighborhood of the target mass and a purely symmetric contribution from very neutron-deficient nuclides. The fission cross sections are extracted by integrating over the reconstructed mass distribution. The width of the mass distribution is determined as a function of target mass. The results for the fission cross sections are compared with other experimental data as well as with theoretical model calculations using the LAHET and the ALICE-91 codes. [S0556-2813(99)07102-2]

PACS number(s): 25.85.Ge, 24.75.+i, 29.30.Kv

I. INTRODUCTION

Since the discovery of fission and the first theoretical description of the mechanism, much has been learned about the fission process and its observables. Both fundamental and applied interests have driven a thorough study of fission of actinides induced by low-energy neutrons. To a lesser extent, also fission reactions induced by neutrons and charged particles at higher incident energies, above, say, 20 MeV, have been investigated. At these higher excitation energies fission of subactinide nuclei becomes possible. Furthermore, the properties of the actinide fission process—like the probabilities of the different fission modes—change and multichance fission becomes more important. This leads, for instance in the case of the actinides, to fragment mass distributions exhibiting a stronger symmetric contribution at higher excitation energies; see, e.g., [1].

Research in the field of high-energy fission is stimulated by the worldwide interest in accelerator-driven systems (ADS's) for transmutation of nuclear waste, energy production, or other purposes. Whereas in most conventional nuclear applications incident particle energies are limited to several MeV, in these ADS concepts energies up to the GeV region play an important role. Feasibility studies of such concepts require knowledge of all the underlying nuclear reactions. Fission of actinides as well as subactinides is a process which is not very well understood at these energies. Compared to spallation and evaporation cross sections the subactinide fission cross section may be small. This contribution should, however, be taken into account for a proper computational analysis of the target and its direct environment, where undesired radioactive isotopes may be produced.

Throughout the years several proton-induced fission experiments have been carried out at energies above 20 MeV. Most of them concern fission of actinides, i.e., Th and U. Many of the measurements on Th have been performed at incident energies below 100 MeV; see, e.g., [2–6]. Only a few data exist in the energy range around 200 MeV; see, e.g., [7,8]. In most of these experiments, no mass distribution but only a very small number of independent isotope yields has been observed in view of charge-dispersion studies. The number of fission experiments in the subactinide region is rather limited. For fission in Pb some experimental results exist for the fission cross section between 70 and 200 MeV [9] and for a modest number of independent and cumulative isotope yields around 500–600 MeV [10,11]. At the ISOLDE facility at CERN, mass and charge distributions of fission fragments have been measured for Pb at 600 MeV [12]. Measurements of residual nuclei produced at the Laboratoire National Saturne and at The Svedberg Laboratory in a large range of projectile energies are described in Refs. [8,13]. However, these experiments have not specifically been designed for fission studies and the number of fission fragments found for incident energies around 200 MeV is rather limited. The same is true for residual nuclei production in W and Au around 200 MeV [8,14]. It is clear that there is a lack of data on light-particle-induced fission at energies above 100 MeV, especially concerning the fission fragment properties.

In order to calculate the fission-product yield data, reliable fission models, which cover a large range of energies and target masses, are needed. Since fission is a relatively slow process, involving a collective deformation of the entire composite nucleus, it is likely to be preceded by a fast, directlike mechanism at high incident energies. After the emission of a few fast particles, the residual nucleus attains an equilibrated state, in which fission may compete with particle evaporation. This immediately illustrates the complexity of the process: a large number of intermediate nuclides, each with its own fission characteristics, are formed in the neighborhood of the target mass. Small deviations in the first stages of the reaction calculation may lead to a very different population of these intermediate nuclides, which contributes

differently to the fission-fragment distribution. This entails that the prediction of high-energy fission yields does not only depend strongly on the fission models, but also on the quality of the models for the direct and preequilibrium part of the reaction that precedes fission and the compound decay that competes with fission.

For the incident energy considered in this paper, the methods to analyze the fast part of the process can be divided in two groups [15]: direct plus preequilibrium models and intranuclear cascade models. Direct and preequilibrium models were originally developed for calculations up to 50 MeV and were later on extended to higher energies. At energies around 200 MeV, secondary and tertiary preequilibrium reactions (emission of two or three fast particles from the composite nucleus) are significant and these mechanisms need to be included to avoid an erroneous prediction of the intermediate residual nuclide population. If a significant amount of energy is carried away by a second or third fast particle, the evaporation chain will stop earlier than when all the intermediate excitation energy is available for compound nucleus decay only. At present, the preequilibrium computer programs give a prediction of the fission cross section but they are not yet able to predict fission-fragment yields.

The alternative approach is provided by the intranuclear cascade model. The classical trajectories of the particles inside the nucleus are followed in coordinate space by means of Monte Carlo methods. When incident nucleon wavelengths are short relative to internucleon distances (i.e., energies in excess of 100 MeV) the collisions of the nucleons can be treated as quasifree scattering processes. In the first stage of the reaction, which is an entirely direct process, the incident particle will cause the knockout of a few intermediate-energy nucleons and other hadrons. This intranuclear cascade stage ends when a residual nucleus with an excitation energy of a few tens of MeV is left, after which the compound stage starts. Some of the intranuclear cascade codes have a preequilibrium model incorporated to describe the transition from the intranuclear cascade stage to the final evaporation stage, in which competition with fission can occur. The fission models give the fission cross section as well as the fission isotope yields. However, these models have been tuned to actinide fission and usually do not perform so well in the case of subactinide fission. Whether to use the preequilibrium approach or the intranuclear cascade approach, and for which energies, is still under debate. The transition regime of validity probably lies somewhere between 100 and 200 MeV. Therefore, we present an analysis by the preequilibrium code ALICE-91 [16] and the intranuclear cascade code LAHET [17].

The absence of a satisfactory theoretical description to predict isotope yields as well as the need for experimental fragment mass and charge distributions forms the motivation for this work, in which we have performed activation experiments for fission studies. A 190 MeV proton beam of the recently built AGOR cyclotron at the KVI, Groningen, has been used to irradiate samples of several target nuclei. By off-line γ-ray spectroscopy the fission products in the irradiated samples have been measured. The use of an advanced catcher system for the fission products, which allows the investigation of the fission process even for lower-Z target materials with a small fission cross section, is treated in Sec. II. Section III describes the simulations, which have been carried out to determine the efficiency of this catcher system. The results of the experiments are presented in Sec. IV. The dependence of the fission process as a function of the target mass has been examined. Moreover, the role of multichance fission has been studied in the case of ^{232}Th. In Sec. V, we compare the results of our measurements with calculations by LAHET and in Sec. VI with the ALICE-91 code. Finally, we give a summary and conclusions in Sec. VII.

II. EXPERIMENTAL SETUP

The stacked foil technique is employed to simultaneously bombard ^{232}Th, ^{208}Pb, ^{nat}Pb, ^{197}Au, and ^{nat}W targets with 190 MeV protons at 10 nA. Two irradiations, one of 5 min and one of 2 h, make it possible to measure both short-lived and long-lived isotopes, with half-lives varying from 5 min up to several years. The identification of the fission products and the determination of their yields is carried out by means of off-line γ-ray spectroscopy with four heavily shielded Ge detectors at KVI and an additional number of counters at ECN. The nuclear data of the γ rays are taken from Ref. [18]. The employed γ-ray energy range of the Ge detectors is 60–3000 keV. The on-average weak samples are placed at small distance to the detectors, which makes a correction of the γ-ray intensities for coincident summing necessary. Flux monitoring is done in two independent ways. A Faraday cup is installed to measure directly the accumulated charge of the beam. The alternative method consists of adding several aluminum foils to the stack. The average proton flux is calculated using the well-known cross section of the ^{27}Al$(p,3p3n)^{22}$Na reaction [19]. Both methods give consistent results. All the uncertainties in our results include a systematical error of 10% due to the uncertainty in the proton flux.

The main task is to separate the desired information in the γ-ray spectra from the background. If the fission cross section has a value much smaller than the total nonelastic cross section, the fission fragments will be drowned in the enormous background caused by contributions of the evaporation residues. This is the case for all the subactinide targets used in this experiment. In order to reduce this background, we have made a catcher system which separates the fission fragments and evaporation residues from each other. Different setups are used for the 5 min and the 2 h irradiation.

A. Long-lived fission products: Catcher foil

For the measurements aiming at the observation of longer-lived fission isotopes, each individual target foil is sandwiched between first a thin ($\sim$0.3 mg/cm^2) and then a thicker ($\sim$3 mg/cm^2) Mylar foil. The thin foil acts as a filter which captures the relatively less energetic evaporation residues, but which transmits most of the fission fragments with their additional energy of $\sim$70 MeV gained from Coulomb repulsion experienced by the two fragments (Fig. 1). The thick Mylar foils trap all fragments which pass the thin ones. After activation they are taken from the stacks and used for further analysis as samples free from evaporation products. We use rather thin targets ($\sim$5 mg/cm^2) to enable a large fraction of the produced fission fragments to escape

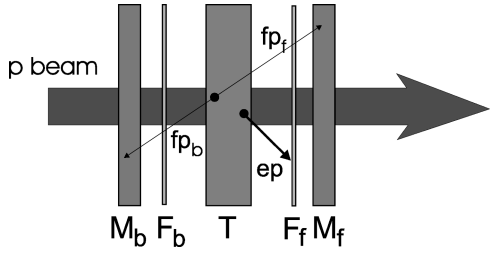

FIG. 1. One target unit with target T sandwiched between filtering foils F_b and F_f in backward and forward positions, respectively. Fission fragments fp are captured in M_b and M_f. Energetic evaporation residues ep cannot pass the filter foils.

them. A disadvantage of this technique is the small absolute yield of the fission fragments per individual target layer, especially for target materials like W, Au, and Pb, which have a fission cross section smaller than 100 mb. In order to improve statistics, a stack of several target units as described above is used. In the present investigation we take around 15 of these units for each target element (Fig. 2). After irradiation the stacks are disassembled, so that corresponding catcher foils can be taken together for subsequent γ-ray spectroscopy. The energy loss of the protons in the total stack has been estimated to be 2.5 MeV.

The setup as described above cannot be used to measure the short-lived fission products. The reason is that the catcher foils are placed in the beam themselves, which causes the protons to interact with the carbon and oxygen in the Mylar, producing overwhelming amounts of the positron-emitting ^{11}C, which has a half-life of 20 min. The intense annihilation radiation from these positrons limits severely the γ-ray spectroscopy during the first hours after the activation. The reactions with C and O furthermore produce ^{7}Be (half-life of 52 days), which emits a gamma of 478 keV, with, fortunately, less detrimental effects on the γ-ray spectroscopy.

B. Short-lived fission products: Catcher cylinder

To obtain access to shorter-lived isotopes it is necessary to prevent the proton beam from interacting with the catcher foils. To achieve this, we have constructed a catcher cylinder, made of polyethylene, as sketched in Fig. 3. A cylinder allows the protons to pass without hitting the catcher itself. The catcher cylinder wall ($\sim$4 mg/cm^2) has full stopping power for all the fission fragments. In this way, we are able to observe fission products with half-lives as short as 5 min

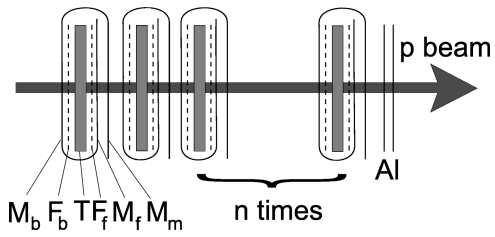

FIG. 2. Stack of target units (see Fig. 1) with an additional Mylar foil M_m to assure separation of individual units. Two Al foils serve for beam-monitoring purposes.

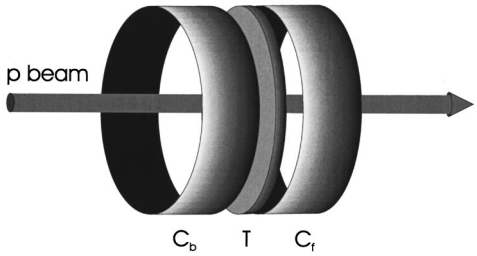

FIG. 3. One target unit with in forward and backward directions a cylindrical catcher for fission fragments, denoted by C_b and C_f.

for ^{232}Th and ^{208}Pb. Because of space limitations in the irradiation chamber, it is not possible to use catcher cylinders for all our targets.

III. SIMULATIONS

In order to extract isotope production cross sections from the data, the efficiencies of the catcher foils and cylinders in collecting the fission fragments must be determined. Simulations with the Monte Carlo code SRIM96 [20] are performed to obtain the efficiencies of the catcher foils. This ion-transport code is based on a fully quantum mechanical treatment of ion-atom collisions. The moving ion undergoes screened Coulomb collisions with the target atoms, which include exchange and correlation interactions between the overlapping electron shells. Furthermore, the ion has long-range interactions, thereby creating electron excitations and plasmons within the target.

For each target, the catcher efficiency has to be determined as a function of the fission-product kinetic energy and mass. The kinetic energy of the fragments is taken from the Viola systematics [21]. Calculations with SRIM96 show that a spread of 0% and of 20% in the kinetic energy distribution has no detectable effect on the total number of fission fragments stopped in the catcher foils. Since the catcher efficiency is merely given by the ratio of collected to produced fission fragments, no spread in the kinetic energy of the fragments is taken into account in the SRIM96 simulations. Furthermore, an isotropic angular distribution for the fragments is assumed, in accordance with the measurements of Bychenkov *et al.* [22]. In Fig. 4 the results of the simulations for the catcher efficiency of a Mylar foil are plotted for a ^{232}Th and a ^{197}Au target. For each target a line is fitted to the simulated data points which is used for interpolation. The overall efficiency is found to be in the order of 30% for a catcher foil. This means that each fission fragment is caught with a total efficiency of 60% in one of the Mylar foils in forward or backward direction with respect to the beam.

Since SRIM96 can only handle flat layers of different materials, another Monte Carlo code GEANT [23] is employed for the more complicated geometry of the catcher cylinder used in the short irradiation setup. GEANT is not specialized in heavy ion transport in matter and not suitable to calculate the transport of the fragments in the target. Therefore, SRIM96 is taken to compute the number of fission fragments coming out of the target. Subsequently, GEANT performs the tracking from the target to the catcher cylinder, which takes place in air. We are only interested in the total number of fission products caught in the cylinder. Because the wall of the

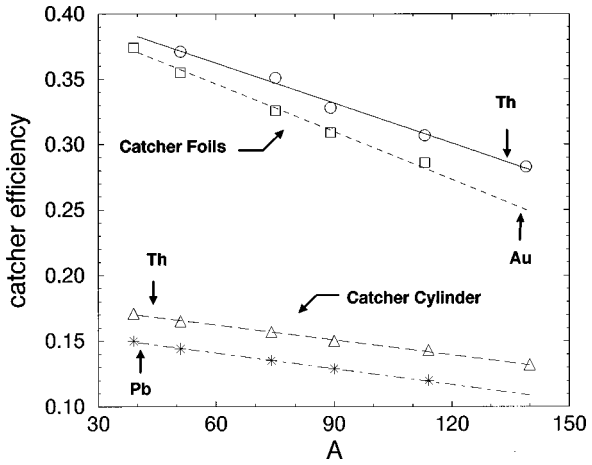

FIG. 4. Catcher efficiency as function of fission-fragment mass A. Circles and squares correspond to the results of SRIM96 simulations for the catcher efficiencies of the Mylar foils (long irradiation) for a thorium and a gold target, respectively. Triangles and stars represent the simulated efficiencies of the catcher cylinders (short irradiation) for a thorium and a lead target, respectively. Lines are fitted to the results of the simulations and are used for interpolation.

catcher cylinder is thick enough to stop all the fragments, it suffices to determine the number of fission fragments that hit the catcher wall with GEANT. The results for ^{232}Th and ^{208}Pb can also be found in Fig. 4. The average efficiency for a catcher cylinder is computed to be 15%.

IV. EXPERIMENTAL RESULTS

A. Isotope yields

At the incident energy considered in this paper, fission fragments are produced in the vicinity of or even in the valley of stability. This is not surprising, because we envisage the fission event to be preceded by preequilibrium emission and evaporation. For the heavy targets studied here, this emission will mainly involve neutrons. Consequently, the neutron-rich fission products linked with low-energy fission of actinides will be less prominent here. Instead, a high yield of stable or extremely long-lived isotopes among the fission products is expected. These nuclei escape our detection method—just like nuclei that do not emit detectable γ rays—leading to incomplete measured yields in many mass bins. But the on-average longer half-lives of the less neutron-rich fission products also give rise to an advantage. Part of the primary fission products, which remain after post-fission neutron evaporation by the fragments, occurs with longer and easier to observe half-lives. They can now be measured directly, instead of only through their beta decay products.

The detected yield of a fission product is called ''cumulated'' if it encompasses the yield of unobserved β-decaying parents, so that it corresponds to a summation of the yields in the beta decay chain with the observed nuclide as end point. A yield is ''independent'' if it represents in essence the primary yield of a fission product. There are two situations in which independent yields can be determined: first, if an isotope is found to be sandwiched in the isobaric chain between two stable or very long-lived nuclides and, second, if both a mother and a daughter nuclide are found. The yield of the daughter, which can be extracted from the data by correcting for the contribution of the mother to the activity of the daughter, is then also independent.

Fission fragments going in backward or forward direction with respect to the proton beam are collected on separate foils or cylinders. Therefore, distinct production cross sections of fission fragments in the backward and forward direction are obtained. The yields turn out to be independent of the direction within the experimental uncertainties, which confirms the assumption made in the simulations that the angular distribution of the fragments is isotropic.

In Table I the fission-product yields obtained for all targets and observed with half-lives covered by our two methods are given. An index *i* in the brackets denotes an independent or a nearly independent yield. In the case of ^{82}Br, for example, the measured ground-state yield corresponds to the sum of the independent ground-state yield and of the almost complete independent isomeric yield. These nearly independent yields reflect the complete independent isotope yield within the experimental uncertainty limits. An index *c* indicates cumulative production cross sections. For several isotopes found, the measured yields are neither independent nor cumulative, because they correspond to only part of the cumulative yield in the mass chain up to that isotope. Some yields given in Table I belong exclusively to the ground state or to the isomeric state of the isotope.

B. Subactinide fission: Mass distributions and fission cross sections

For each subactinide target the mass distribution is extracted from the measured cumulative and independent isotope yields (marked with *c* and *i*, respectively, in Table I) by fitting simultaneously the mass and charge distribution. The fission process is assumed to be symmetric for the subactinide targets. The mass and charge distributions are, therefore, both described with a single Gaussian in the fit. Moreover, we assume that the most probable charge Z_p as well as the width of the charge distribution Γ_Z varies linearly with the mass of the fission fragment. In this way, we arrive at the following parametrization of the production cross section σ_{prod} (A,Z) as a function of the mass and charge of the fission fragment:

$$\sigma_{\mathrm{prod}}(A,Z)=\lambda_A\ e^{-(A-M_A)^2/\Gamma_A^2}\frac{1}{\sqrt{\pi}\Gamma_Z}\sum_i\ e^{-(Z-i-Z_p)^2/\Gamma_Z^2}, \tag{1}$$

with $Z_p=\mu_1+\mu_2 A$ and $\Gamma_Z=\gamma_1+\gamma_2 A$. The first Gaussian represents the symmetric mass distribution defined by a height λ_A, a mean M_A, and a width Γ_A. The rest of the formula reflects the charge distribution. In the case of an independent yield, only one term in the sum of the normalized Gaussian charge distribution (i.e., $i=0$) contributes. A cumulative yield is described by summing the contributions of neighboring isobars. The index *i* is equal to 0,1 . . . ,5 for neutron-rich cumulative yields and equal to $0,-1\ldots,-5$ for neutron-poor cumulative yields. The number of six terms in the summation for cumulative yields is rather arbitrary, but in our investigations it has turned out to be sufficient. For

TABLE I. Fission-product isotope yields resulting from 190 MeV proton-induced reactions as measured for the targets ^{nat}W, ^{197}Au, ^{208}Pb, ^{nat}Pb, and ^{232}Th. The half-lives and the production cross sections are given. The *i* and *c* in parentheses denote independent and cumulative yields, respectively, of the isotope, its ground state, or its isomer as given.

Isotope		Half-life	^{nat}W [mb]	^{197}Au [mb]	^{208}Pb [mb]	^{nat}Pb [mb]	^{232}Th [mb]
^{59}Fe	(c)	45.1 d	0.053±0.008	-	-	-	-
^{67}Cu	(c)	61.9 h	0.075±0.008	0.25±0.03	0.28±0.04	0.36±0.04	0.61±0.07
^{69m}Zn	(i)	13.8 h	0.036±0.005	0.171±0.019	0.27±0.04	0.18±0.03	0.20±0.03
^{71m}Zn	(i)	3.9 h	-	0.122±0.013	-	0.152±0.017	-
^{72}Zn	(c)	46.5 h	0.0169±0.0019	0.118±0.013	0.20±0.03	0.27±0.03	10.28±0.14
^{72}Ga	(i)	14.1 h	0.064±0.013	0.14±0.05	0.29±0.06	0.16±0.04	0.24±0.07
^{73}Ga	(c)	4.86 h	0.040±0.004	0.30±0.03	0.50±0.07	0.36±0.03	-
^{74}Ga	(c)	8.1 min	-	-	0.43±0.11	-	-
^{74}As	(i)	17.8 d	0.040±0.006	0.167±0.025	-	0.101±0.012	-
^{75}Se	(c)	120 d	-	0.084±0.011	-	0.036±0.007	-
^{76}As	(i)	26.4 h	0.085±0.012	0.38±0.04	0.36±0.06	0.46±0.07	-
^{77}Ge		11.3 h	-	-	0.23±0.03	0.230±0.023	1.35±0.11
^{77}Br	(c)	57.0 h	0.033±0.007	0.098±0.018	-	-	-
^{78}Ge	(c)	88.0 min	-	-	0.22±0.04	-	5.9±1.3
^{78}As	(c/i)	1.5 h	-	0.32±0.03 (c)	0.61±0.24 (i)	0.39±0.12 (i)	-
^{81m}Se		57.3 min	-	0.27±0.05	0.92±0.14	-	-
^{82}Br	(i)	35.3 h	0.089±0.014	0.77±0.14	1.20±0.15	1.67±0.14	-
^{83}Rb	(c)	86.2 d	0.077±0.010	0.29±0.03	-	0.200±0.022	0.078±0.008
^{84}Br		31.8 min	-	-	-	-	13±3
^{84}Rb	(i)	32.8 d	0.085±0.010	0.56±0.06	-	0.57±0.06	0.28±0.03
^{85}Sr		64.9 d	0.068±0.009	0.273±0.029	-	0.189±0.020	-
^{86}Rb	(i)	18.7 d	0.19±0.03	1.08±0.12	-	2.21±0.23	1.56±0.14
$^{87g.s.}$Y		80.3 h	0.008±0.006	-	0.120±0.021	0.121±0.013	-
^{87m}Y		13.0 h	0.029±0.004	0.149±0.021	-	0.081±0.015	-
^{87}Kr	(c)	76.3 min	-	-	-	-	5.7±1.3
^{88}Y	(c)	106.6 d	0.083±0.013	0.58±0.06	-	0.51±0.05	0.252±0.026
^{89}Rb	(c)	15.2 min	-	-	1.4±0.3	-	25±5
^{89}Zr	(c)	78.4 h	0.029±0.003	0.123±0.013	-	0.069±0.008	0.099±0.010
^{90m}Y	(i)	3.19 h	0.112±0.018	0.66±0.05	1.5±0.3	0.99±0.16	2.7±00.6
^{91}Sr	(c)	9.5 h	-	0.48±0.08	2.06±0.22	1.10±0.12	13.6±1.4
^{91m}Y	(i)	49.7 min	-	-	2.3±0.5	-	7.1±1.5
^{92}Sr	(c)	2.71 h	-	0.169±0.021	1.71±0.24	0.53±0.05	38±8
^{92}Y	(i)	3.54 h	-	0.76±0.3	1.6±0.8	1.17±0.20	-
^{92m}Nb	(i)	10.2 d	-	-	0.09±0.02	-	-
^{93}Y	(c)	10.2 h	-	-	1.66±0.26	0.99±0.10	14.1±1.6
^{94}Y	(c)	18.7 min	-	-	1.8±0.4	-	27±6
^{95}Zr	(c)	64.0 d	0.056±0.008	0.77±0.06	3.3±0.3	3.32±0.25	23.7±1.7
^{95}Nb	(i)	35.0 d	0.093±0.025	0.90±0.25	1.6±0.3	1.68±0.25	-
^{96}Nb	(i)	23.4 h	-	0.96±0.15	1.6±0.3	1.68±0.12	3.2±0.3
^{96}Tc	(i)	4.3 d	0.0160±0.0018	-	-	-	0.93±0.10
^{97}Zr	(c)	16.8 h	-	0.163±0.021	1.21±0.17	1.21±0.18	36±8
^{97}Nb	(i)	74.0 min	-	0.49±0.15	2.4±0.8	1.26±0.14	14±5
^{98m}Nb	(i)	51.0 min	-	0.27±0.03	-	0.67±0.07	14±7
^{99}Mo	(c)	66.0 h	0.072±0.012	0.93±0.17	3.7±0.5	3.2±0.3	24.4±1.8
^{99m}Tc	(i)	6.0 h	0.008±0.003	0.14±0.04	0.25±0.08	0.057±0.010	-
^{101}Mo	(c)	14.6 min	-	-	2.2±0.4	-	62±11
^{101}Tc	(i)	14.2 min	-	-	2.8±1.0	-	-
^{102m}Tc	(i)	4.3 min	-	-	0.78±0.27	-	-
^{103}Ru	(c)	39.4 d	0.089±0.010	1.23±0.19	4.5±0.5	4.9±0.4	29±3
^{104}Tc	(c)	18.2 min	-	-	1.24±0.22	-	31±5
^{105}Ru	(c)	4.40 h	-	0.45±0.04	2.5±0.3	1.28±0.09	59±13
^{105}Rh	(c/i)	35.5 h	0.077±0.015 (c)	0.75±0.12 (i)	2.0±0.5 (i)	1.8±0.6 (i)	10±3 (i)

TABLE I. *(Continued).*

Isotope		Half-life	^{nat}W [mb]	^{197}Au [mb]	^{208}Pb [mb]	^{nat}Pb [mb]	^{232}Th [mb]
^{106}Ru	(c)	368 d	-	-	-	0.86±0.10	19.9±2.2
^{106m}Rh	(i)	2.2 h	-	0.27±0.03	0.40±0.07	0.51±0.05	-
^{107}Rh	(c)	21.7 min	-	-	2.5±0.5	-	58±9
^{108m}Rh	(i)	5.9 min	-	-	0.60±0.21	-	-
^{109m}Pd	(i)	4.69 min	-	-	0.58±0.21	-	-
^{110m}Ag	(i)	250 d	-	0.39±0.04	-	1.09±0.10	2.10±0.16
^{111m}Pd		5.5 h	-	-	0.58±0.08	0.37±0.03	6.2±0.9
^{111}Ag		7.45 d	-	0.51±0.06	2.3±0.5	2.0±0.3	70±16
^{111m}Cd		49.0 min	-	-	0.20±0.03	0.34±0.04	-
^{112}Ag	(c)	3.12 h	-	0.33±0.04	2.7±0.4	1.01±0.09	-
^{113}Ag	(i)	5.37 h	-	-	1.3±0.4	0.73±0.17	21.8±2.5
^{114m}In	(i)	49.5 d	-	0.218±0.025	-	0.62±0.07	1.53±0.16
^{115}Ag	(i)	20.0 min	-	-	-	-	23±5
^{115}Cd		53.4 h	-	0.041±0.003	-	0.49±0.04	18.1±1.4
^{116m}In		54.0 min	-	-	0.43±0.07	0.45±0.06	10±3
^{117}Cd		2.42 h	-	-	-	-	13±3
$^{117g.s.}$In		43.1 min	-	-	0.51±0.10	-	14±4
^{117m}Sn		13.6 d	-	-	0.49±0.07	0.55±0.07	1.57±0.17
^{118m}Sb	(i)	5.0 h	-	-	0.53±0.16	-	-
^{120m}Sb	(i)	5.76 d	-	0.058±0.024	0.50±0.08	0.57±0.08	2.80±0.26
^{121m}Te	(i)	154 d	-	0.078±0.009	-	0.168±0.018	0.44±0.05
^{122}Sb	(i)	2.70 d	-	-	0.60±0.10	0.22±0.03	5.4±0.6
^{123m}Sn		40.1 min	-	-	-	-	8.0±1.7
^{123m}Te		120 d	-	-	-	-	3.0±0.3
^{124}Sb	(i)	60.3 d	-	-	-	0.206±0.021	7.3±1.1
^{124}I	(i)	4.15 d	-	0.025±0.005	0.34±0.10	0.17±0.02	2.6±0.3
^{125}Sn		9.64 d	-	-	-	-	4.6±0.4
^{125}Sb	(c)	2.77 y	-	-	-	-	6.2±1.2
^{126}Sb		12.4 d	-	-	-	-	4.0±0.3
^{126}I	(i)	13.0 d	-	-	-	0.239±0.026	2.5±0.3
^{127}Sb	(c)	3.85 d	-	-	-	-	5.8±0.6
^{128}Sb		9.0 h	-	-	-	-	1.22±0.11
^{129m}Te		33.6 d	-	-	-	-	5.8±0.6
^{129}Cs	(c)	32.1 h	-	-	0.26±0.06	0.22±0.03	0.75±0.09
^{130}I	(i)	12.4 h	-	-	-	-	3.4±0.4
$^{131g.s.}$Te		25.0 min	-	-	-	-	4.1±0.9
^{131m}Te		30.0 h	-	-	-	-	5.4±1.2
^{132}Te	(c)	76.3 h	-	-	-	-	3.2±0.3
^{132}Cs	(i)	6.47 d	-	-	-	0.116±0.012	-
^{133}I	(c)	20.8 h	-	-	-	-	5.1±0.5
^{133}Ba	(c)	10.5 y	-	-	-	-	0.98±0.14
^{134}Cs	(i)	2.06 y	-	-	-	-	3.0±0.3
^{135m}Cs	(i)	53.0 min	-	-	-	-	10.5±2.2
^{136}Cs	(i)	13.2 d	-	-	-	-	3.3±0.3
^{137m}Ce		34.4 h	-	-	-	-	3.4±0.4
^{139}Ba	(c)	83.1 min	-	-	-	-	14±3
^{139}Ce	(c)	138 d	-	-	-	-	1.22±0.13
^{140}Ba	(c)	12.8 d	-	-	-	-	6.5±0.6
^{140}La	(i)	40.3 h	-	-	-	-	2.6±0.9
^{141}Ce	(c)	32.5 d	-	-	-	-	9.2±1.0
^{143}Ce	(c)	33.0 h	-	-	-	-	3.5±0.4
^{144}Ce	(c)	284.8 d	-	-	-	-	5.2±0.5

TABLE II. Fit parameter values obtained for a single Gaussian for the different targets [Eq. (1)]. The mass distribution is described by a Gaussian with the parameters λ_A for the height, M_A for the mean, and Γ_A for the width. The charge distribution is also given by a Gaussian, with the width given as $\Gamma_Z = \gamma_1 + \gamma_2 A$ and the most probable charge as $Z_p = \mu_1 + \mu_2 A$. Fission cross sections are compared with values obtained from the fit of Eismont *et al.* [25]. The uncertainties in the fit parameters denote the sensitivity of the fit. The uncertainties in the fission cross sections include a 10% systematical error.

	^{nat}W	^{197}Au	^{nat}Pb	^{208}Pb
λ_A	0.2323±0.0022	2.085±0.011	5.88±0.26	5.0±0.7
M_A	87.1±0.2	92.2±0.1	99.5±0.4	100.7±0.8
Γ_A	22.1±0.3	17.7±0.1	18.1±0.3	19.8±0.6
γ_1	0.801±0.010	0.850±0.005	0.74±0.10	0.5±0.3
γ_2	0.0051±0.0004	0.00395±0.00022	0.0046±0.0014	0.008±0.004
μ_1	1.619±0.007	1.642±0.005	1.18±0.08	0.97±0.18
μ_2	0.4147±0.0002	0.41193±0.00010	0.4137±0.0009	0.413±0.002
$\sigma_f^{\text{our expt}}$ [mb]	4.5±0.5	32.8±3.3	94±9	88±8
$\sigma_f^{\text{Eismont}}$ [mb]	3.7	-	88	74

a more elaborate description of the functional form we refer to the work of Hagebø and Lund [12].

The values of the fit parameters obtained for all subactinide targets are tabulated in Table II. The mean value as well as the height of the mass distribution clearly increases with increasing target mass, as expected. From the mean of the mass distributions it can be concluded that on the average nine mass units are emitted before and after fission. The relative width Γ_A/A of the mass distribution is shown in Fig. 5 as a function of the fissility parameter Z^2/A. This quantity increases in going from ^{nat}Pb to ^{nat}W. The wider distribution of ^{nat}W is in agreement with the observation by Becchetti *et al.* [24] and others that the relative widths of the fission-fragment mass distribution increase with decreasing target mass.

With the charge distribution known from the fit of expression (1), it is straightforward to determine the fractional chain yield represented by each of the observed independent or cumulative isotope yields in their mass chains. Subsequently, the measured yields are divided by their fractional chain yield to derive the experimental mass yields. In the case of ^{nat}Pb the spread in the corrected yields is rather large.

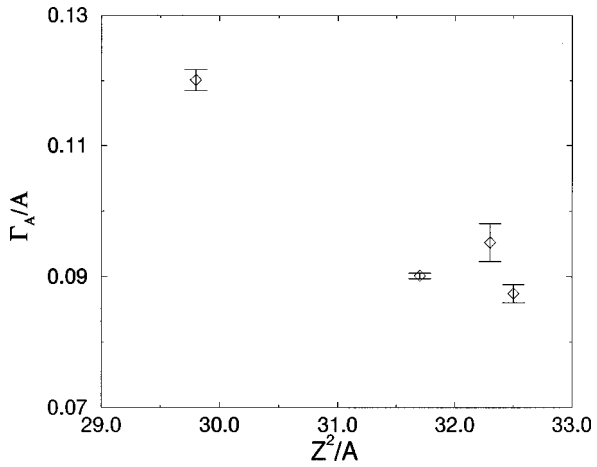

FIG. 5. Relative Gaussian width, defined as Γ_A/A, of the fission-product mass distributions as a function of the fissility parameter Z^2/A.

Therefore, the final mass distribution has been obtained after fitting to the measured yields which represent at least 50% of the complete mass yield. In Fig. 6 the complete mass yields are plotted together with the mass distribution obtained in the fit for ^{nat}W, ^{197}Au, ^{nat}Pb, and ^{208}Pb. The results confirm our assumption of a symmetric mass and charge distribution.

Integrating over the Gaussian and multiplying with a factor $\frac{1}{2}$, because of the two fission fragments in each fission event, gives an estimate for the fission cross section. The values for the fission cross sections determined in this way are also given in Table II. Eismont *et al.* [25] have made a data compilation for the fission cross section as a function of incident proton energy for some of these target materials. The values from the fit of Eismont *et al.* are also shown in Table II for comparison and are in fairly good agreement with our results. In the case of ^{nat}Pb the fissioning systems are on the average farther away from the double magic nucleus ^{208}Pb, which should give rise to a higher fission cross section for ^{nat}Pb. According to the calculations made with the ALICE-91 code in Sec. VI, this effect is of the order of 10%, which corresponds to the experimental uncertainty. From our results it is, therefore, impossible to draw a conclusion concerning a difference between ^{nat}Pb and ^{208}Pb.

Contributions of asymmetric and symmetric fission in ^{232}Th

When we fit the expression (1) to the measured yields of ^{232}Th, we arrive at the mass yields and the mass distribution as pictured in Fig. 7. The result is not a Gaussian with the data falling nicely on top of it, as is the case for the subactinide targets. Furthermore, we obtain a fission cross section of 630±60 mb, which is much lower than the value of Eismont *et al.* of 1236 mb. The values of the fit parameters can be found in Table III. Looking carefully at the ^{232}Th mass yields, one notices a dip in the yields around fragment mass 125. We therefore suggest that the fragment mass distribution for ^{232}Th cannot be properly described by a single Gaussian, but is instead a superposition of a wide flattened distribution and a narrower Gaussian. This more complicated

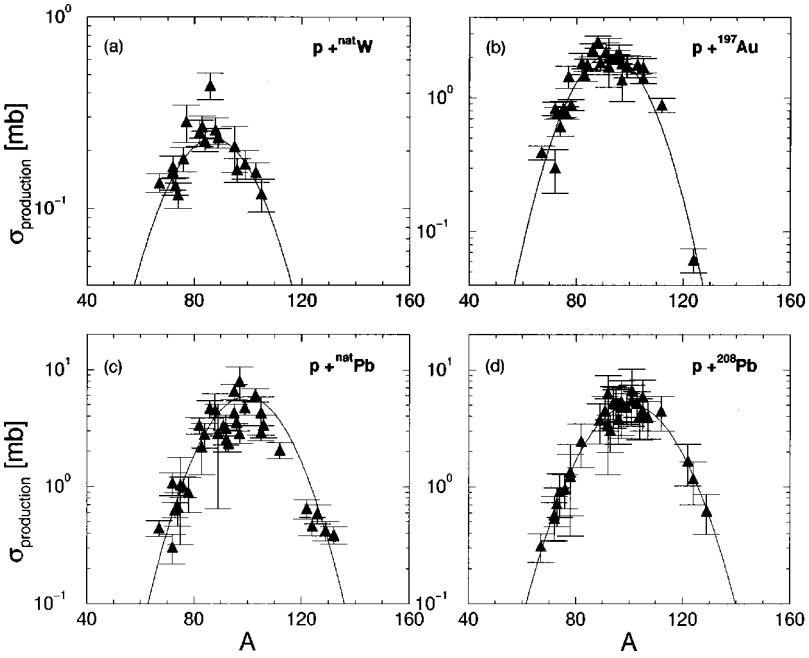

FIG. 6. Fission-product mass yields from 190 MeV proton-induced fission on ^{nat}W (a), ^{197}Au (b), ^{nat}Pb (c), and ^{208}Pb (d). The lines indicate the fitted Gaussian mass distributions; the triangles correspond to the experimental mass yields.

form of the mass distribution can stem from contributions by different fissioning mechanisms in the many fissioning intermediate nuclides.

Because of the particle evaporation process that takes place before fission, there exists a set of various fissioning nuclides. Each of them has its own fission characteristics and excitation energy and angular momentum distributions. Chung and Hogan [26,27] have collected data on the mass yield curves for fissioning nuclei with atomic numbers ranging from $Z=80$ to $Z=105$. They propose that nuclides with a fissility parameter Z^2/A greater than a critical value $(Z^2/A)_C$ are situated in the region of symmetrical fission, while nuclides with Z^2/A smaller than that value fission only asymmetrically. Their approach is based on the observation that the symmetric component increases with excitation energy. A higher excitation energy is coupled to an increase of neutron evaporation, resulting in a larger contribution of the neutron-deficient nuclides with higher fissility parameter. From the data they have extracted an expression for this critical value as a function of nuclide charge:

$$(Z^2/A)_C = 35.5 + 0.4(Z-90). \tag{2}$$

Measurements of proton-induced fission of ^{232}Th between 8 and 22 MeV have been performed by Kudo *et al.* [28]. According to the assumption made by Chung and Hogan the

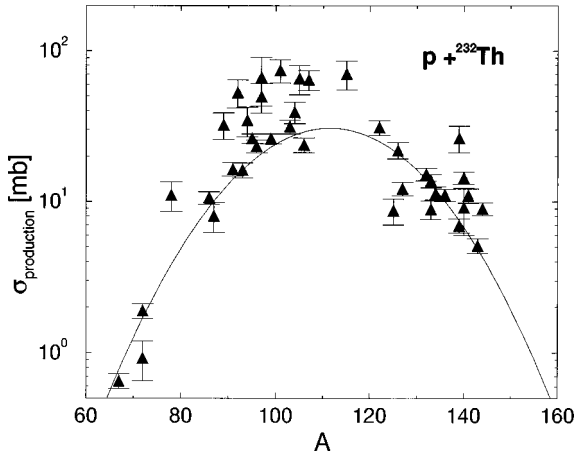

FIG. 7. Same as Fig. 6, but for ^{232}Th. Experimental mass yields obtained from the parametrization of Eq. (1) are not described in a satisfactory way by the Gaussian.

TABLE III. Fit parameter values for the ^{232}Th mass yield curves. The first two columns contain the values of the fit parameters for the single-Gaussian mass and charge distribution fit (referred to as symmetric). In the third and fourth columns the parameter values that describe the decomposition of the mass distribution can be found (referred to as decomposed). The meaning of the parameters is explained in the text. The fission cross sections as obtained from the fit parameters are given as well as the value of Eismont *et al.* The uncertainties in the fit parameters denote the sensitivity of the fit. The uncertainties in the fission cross sections include a 10% systematical error.

Symmetric fit parameters	Value	Decomposed fit parameters	value
λ_A	30.7 ± 0.5	$s1$	52 ± 4
M_A	111.5 ± 0.2	$s2$	107.3 ± 0.4
Γ_A	23.15 ± 0.14	$s3$	14.7 ± 0.6
-	-	$m1$	5.3 ± 1.0
-	-	$m2$	110.0 ± 0.3
-	-	$m3$	30.2 ± 2.2
-	-	$m4$	11.2 ± 0.7
-	-	$m5$	27.7 ± 0.3
-	-	$m6$	6.5 ± 0.4
γ_1	0.820 ± 0.012	γ_1	0.345 ± 0.012
γ_2	0.00786 ± 0.00013	γ_2	0.0129 ± 0.0002
μ_1	1.92 ± 0.02	μ_1	2.07 ± 0.02
μ_2	0.3910 ± 0.0002	μ_2	0.38953 ± 0.0004
$\sigma_f^{\text{our expt}}$ [mb]	630 ± 60	$\sigma_f^{\text{our expt}}$ [mb]	950 ± 95
$\sigma_f^{\text{Eismont}}$ [mb]	1236	$\sigma_f^{\text{Eismont}}$ [mb]	1236

mass distributions in their experiment should be purely asymmetric, since all the fissioning systems contributing have a Z^2/A smaller than the critical value. But the mass distribution in their experiment turns out to have a symmetric contribution as well. Therefore, we assume that fissioning nuclides like ^{232}Th and adjacent isotopes are responsible for a mass yield curve which is wide and to some extent flattened, due to the mixed contributions from asymmetric and symmetric fission modes (referred to as mixed fission). Furthermore, we assume that the very neutron-deficient lighter isotopes of Th and of the neighboring lower-Z elements produce a reasonably narrow Gaussian mass distribution, belonging to a symmetric fission mode only (referred to as purely symmetric fission). This idea arises also from the observation that the narrower Gaussian in the experimental mass distribution seems to be shifted to lower masses in comparison to the wide and flattened part of the mass distribution. An experiment by Schmidt *et al.* [29] on fission of neutron-deficient actinides shows indeed a transition of a mixed to a symmetrical charge distribution with decreasing neutron number.

It is possible to decompose the mass yield curve observed for ^{232}Th on basis of the assumptions described above by splitting the dependence on the fission-fragment mass of the production cross section in a part for purely symmetric and in a part for mixed fission:

$$\sigma_{prod}(A,Z) = \Big[\underbrace{s_1\, e^{-\frac{(A-s_2)^2}{s_3^2}}}_{symmetric} + \underbrace{m_1\, e^{-\frac{(A-m_2)^2}{m_3^2}} + m_4\, e^{-\frac{(A-(m_2-m_5))^2}{m_6^2}} + m_4\, e^{-\frac{(A-(m_2+m_5))^2}{m_6^2}}}_{mixed} \Big] \cdot \frac{1}{\sqrt{\pi}\Gamma_Z} \sum_i e^{-\frac{(Z-i-Z_p)^2}{\Gamma_Z^2}}, \tag{3}$$

with A and Z being the fragment mass and charge, $s_{1,\ldots,3}$ the fit parameters of the purely symmetric fission contribution, and $m_{1,\ldots,6}$ the fit parameters of the mixed fission contribution. The mixed fission parametrization consists of three Gaussians, the first Gaussian describing the symmetric and the other two describing the asymmetric fission contribution. Although we assume the fission process to be a sum of symmetric and mixed contributions, we take the charge dependence the same as in expression (1). An attempt to take a more general form of the charge distribution into account, consisting of a sum two Gaussians, failed because the experimental data are not sufficient to reconstruct a more complicated form. The values of the fit parameters can be found in Table III.

The result for the mass distribution is given in Fig. 8. The triangles denote the experimental values that are corrected using the fractional chain yields determined with the charge distribution from the fit. The observed points that correspond to less than 10% of the complete mass yields are left out in the final fit. The spread in the complete mass yields may be due to the use of the simplified parametrization of the charge distribution. Adding the mixed and the purely symmetric contributions results in a mass yield curve that resembles the measured form of the mass distribution better than the single-Gaussian fit of Eq. (1). The purely symmetric Gaussian has a smaller mean value than the Gaussian that represents the symmetric component of mixed fission. This is in agreement with the idea that the purely symmetric Gaussian comes from the fissioning nuclides that have lost more prefission neutrons. The four Gaussians give only a schematic description of reality, but it enables us to estimate the part of the fission cross section originating from purely symmetric and from mixed fission. A disentanglement of the contributions of the different fission modes in all the fissioning nuclides is far more complicated. From this decomposition we

TABLE IV. Purely symmetric and the mixed fission cross sections in proton-induced reactions on ^{232}Th at 190 MeV as determined from the experimental data and from the LAHET and ALICE-91 calculations.

	$\sigma_f^{\text{symmetric}}$ [mb]	σ_f^{mixed} [mb]
Experimental	680±70	271±27
LAHET	687	372
ALICE-91	796	361

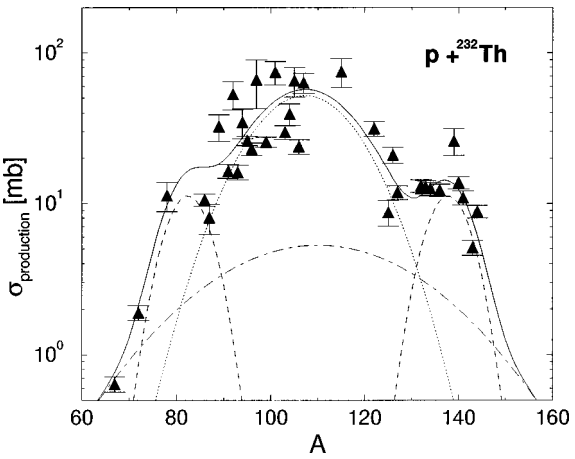

FIG. 8. Decomposition of the ^{232}Th mass yield curve into one Gaussian (dotted line), coming from purely symmetric fission of lighter nuclides, and three Gaussians representing the mixed symmetric (dot-dashed line) and asymmetric (dashed line) fission modes of heavier nuclides. The solid line indicates the sum of the symmetric and the mixed contributions. Triangles represent the experimental mass yields resulting from dividing the measured yields by the fractional yields obtained with Eq. (3).

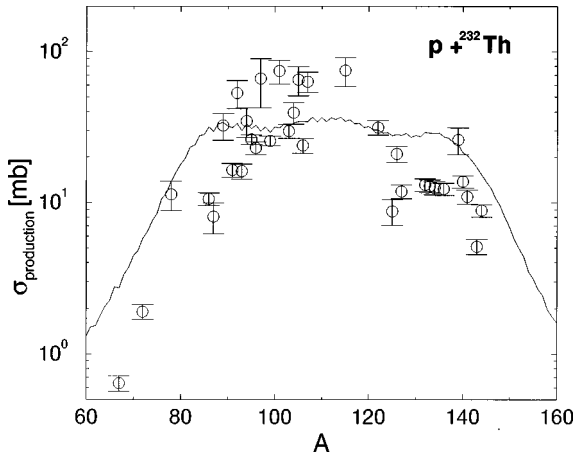

FIG. 9. Experimental mass yields for 190 MeV proton-induced fission of ^{232}Th (circles). The curve for complete fission yields has been calculated with LAHET.

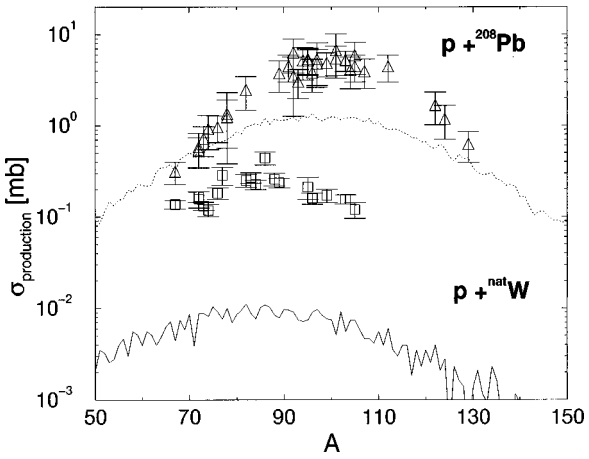

FIG. 10. Same as Fig. 9 for ^{208}Pb (triangles and dotted curve) and ^{nat}W (squares and solid curve).

estimate a cross section of 680 ± 70 mb for purely symmetric and 271 ± 27 mb for mixed fission. The new total fission cross section thus becomes 950 ± 100 mb, which is in better agreement with the value of Eismont *et al.* of 1236 mb than the value originating from the single-Gaussian fit. We conclude, therefore, that a decomposition of the ^{232}Th fission fragment mass distribution into a mixed fission and a purely symmetric fission component gives a better description of the data than a single Gaussian. A comparison of the symmetric fission cross section and the mixed fission cross section with theoretical calculations is presented in Secs. V and VI.

The previously mentioned experiment by Schmidt *et al.* [29] supports our assumptions on the mixed and purely symmetric fission components. Other experimental evidence for the form of the fission-product mass distribution can be found in the work by Pappas and Hagebø [30] and by Lee *et al.* [31]. Pappas and Hagebø arrived at similar findings when inducing fission of ^{238}U with 170 MeV protons. They have proposed a decomposition of the mass yield curve into a symmetric contribution caused by high-deposition-energy events, and two asymmetric contributions connected to low- and high-deposition-energy events. Lee *et al.* have studied fission in the bombardment of ^{238}U with 240 MeV ^{12}C ions. They have interpreted the mass distribution as a superposition of three components: asymmetric low-energy fission, symmetric high-energy fission (a combination of fusion-fission and fast fission), and symmetric sequential fission (i.e., fission preceded by multiple nucleon emission). What these two approaches have in common with our work is the symmetric component linked with the more neutron-deficient fissioning systems. However, the interpretation concerning the contributions of the less neutron-poor nuclides is different. We assume that both symmetric and asymmetric fission modes play a role in this region of nuclides close to the valley of stability, while Pappas and Hagebø omit the symmetric fission contribution completely and Lee *et al.* neglect the asymmetric fission contribution for excitation energies above 35 MeV (although, according to theoretical calculations, the shell effects responsible for asymmetric fission have not yet vanished at these energies; see, e.g., [32]).

V. LAHET CALCULATIONS

We calculate fission-fragment mass distributions with the Monte Carlo high-energy transport code LAHET [17]. In LAHET a nuclear interaction is treated in the following steps. It starts with an intranuclear cascade, for which the Bertini model is utilized. Subsequently, a multistage exciton model is employed to compute the preequilibrium part of the reaction. Finally, the compound stage is calculated with an evaporation model. During this last step of the calculation fission can be included. We use the Rutherford Appleton Laboratory (RAL) model by Atchison [33] to describe the fission process, because it allows for fission of elements with atomic number as low as $Z=71$. In fact the RAL model consists of two models, one for actinide and another for subactinide fission. The actinide fission model is semiphenomenological and is based on the observation that the fission probability above a certain excitation energy of the nucleus becomes more or less constant. In the case of subactinide fission the widths for neutron evaporation and fission are obtained from the statistical model for fission. An empirical relation is used to determine, subsequently, the mass distribution. For a more detailed treatment we refer to Ref. [33].

In Fig. 9 and Fig. 10 the results of the LAHET calculations are shown together with the experimental complete mass yields for ^{nat}W (squares), ^{208}Pb (triangles), and ^{232}Th (circles). The fluctuations in the calculated mass yields are caused by poor statistics. Although 1×10^6 events are taken for ^{232}Th and ^{208}Pb and even 10×10^6 events for ^{nat}W, the resulting statistics for the fission results is low due to the small cross sections.

With LAHET we arrive at a description of the proton-induced fission of ^{232}Th resulting in a broad distribution which is rather flat. This is the expected result of the mixed symmetric and asymmetric fission. However, the purely symmetric component of the very neutron-deficient nuclides does not show up in the mass distribution. The fission cross section for ^{232}Th as calculated by LAHET is 1059 mb, which agrees with our value of 950 ± 100 mb. This means that the widths for fission and neutron evaporation—determining the moment of fission in the evaporation chain—used for ^{232}Th give a result consistent with the experiment, whereas the subsequent calculation of the fission fragment properties

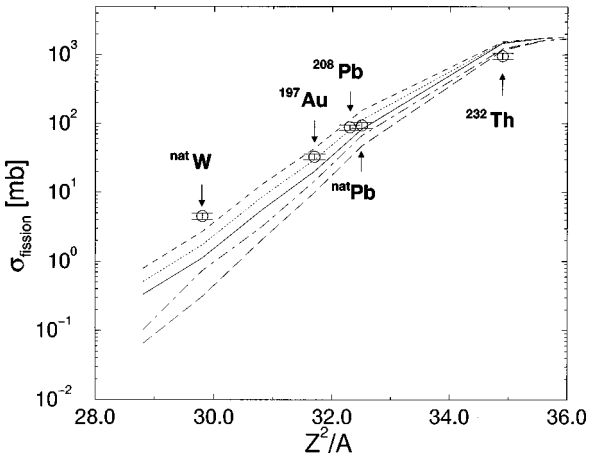

FIG. 11. Fission cross sections as a function of fissility parameter calculated by ALICE-91 with the rotating finite range model (RFRM) of Sierk for $a_f/a_n=1.00$ (solid line), 1.01 (dotted line), and 1.02 (dashed line) and with the rotating liquid drop model (RLDM) for $a_f/a_n=1.00$ (long-dashed line) and 1.01 (dot-dashed line). The computational results are compared with the experimental values obtained in the present work.

does not yield the experimental form of the mass distribution. It is possible to extract the contribution to the fission cross section per fissioning nucleus in LAHET. All fissioning nuclides are divided into a purely symmetric group and a mixed fission group according to the condition given in Eq. (2) and their respective contributions to the fission cross section are added. The results obtained in this manner are shown in Table IV. The values deduced from the experimental data are given in this table as well for comparison. The calculated mixed fission cross section is somewhat higher than our experimental value. But when one bears in mind the schematical nature of the decomposition we make for the thorium mass yield distribution, the agreement with the experimental values from Sec. IV is surprisingly good.

Figure 10 reveals a large discrepancy between the predictions for subactinide fission by LAHET and the experimental data. The fission cross sections are 32 mb and 0.26 mb for ^{208}Pb and ^{nat}W, respectively. This implies a large underestimation of the experimental values: 88 ± 8 mb for ^{208}Pb and 4.5 ± 0.5 mb for ^{nat}W. Furthermore, the widths of the mass distributions are too large.

VI. ALICE-91 CALCULATIONS

We also perform fission cross-section calculations with the precompound plus compound nucleus decay code ALICE-91 developed by Blann [16]. The geometry-dependent hybrid (GDH) model is employed in the preequilibrium part of the reaction. In this model the diffuseness of the nuclear surface is taken into account. This leads to an enhancement of peripheral collisions undergoing precompound decay, thereby depleting the higher angular momenta more than in the conventional hybrid model. Reduction of angular momentum by particle evaporation is also taken into account. The compound part of the reaction is computed using Weisskopf-Ewing evaporation with fission competition via the Bohr-Wheeler approach, in which the fission process is described by a passage probability of the nucleus over the classical fission saddle point. Angular-momentum-dependent fission barriers and ground-state energies are supplied by the rotating finite-range model (RFRM) of Sierk [34]. This model is based on calculations that include finite-range effects in the nuclear surface energy and finite surface-diffuseness effects in the Coulomb energy and in the rotational moments of inertia. If the angular momentum is larger than a critical value, the fission barrier is taken to be zero. For comparison, the calculations are repeated with fission barriers and ground-state energies provided by the rotating-liquid-drop model (RLDM).

The fission cross section computed with ALICE-91 is, apart from depending on the model, also dependent on the choice for a_f/a_n, being the ratio of saddle-point to ground-state level densities. Because of the (stronger) deformation at the saddle point, this ratio is expected to be slightly larger than 1.00. The results for calculations of the fission cross section with the RFRM for $a_f/a_n=1.00$, 1.01, and 1.02 are drawn in Fig. 11 as a function of the fissility parameter Z^2/A. Results are also shown of computations with RLDM quantities for the values $a_f/a_n=1.00$ and 1.01. The measured fission cross sections are denoted by the circles in Fig. 11.

The subactinide fission cross sections are best reproduced with the RFRM by Sierk. A well-known property of the RLDM is the overestimation of the fission barriers for nuclei with mass number less than about 200, resulting in an underprediction of the fission cross sections. This problem can be solved either by using an extra scaling factor to reduce the fission barrier or by increasing a_f/a_n to enhance the fission process at the expense of the evaporation process. We find that a best description in the subactinide range of Z^2/A is offered by $a_f/a_n=1.01$ and 1.02 with the RFRM. Our value of a_f/a_n is considerably smaller than the value of 1.05 as used in ALICE-91 calculations of proton-induced fission cross sections at 190 MeV with RLDM barriers by Becchetti *et al.* [24], as we expect from the argument given above. In their calculations as well as in ours, it seems that a better fit with the data is obtained with a lower value of a_f/a_n for heavier target elements ($a_f/a_n\sim1.01$, in our case) and with a somewhat higher value for the lighter target elements ($a_f/a_n\sim1.02$, in our case).

In the actinide region we only have one point, namely, for ^{232}Th. For this isotope we find that the RLDM gives the best agreement with the experimentally found fission cross section for ^{232}Th. As can be seen in Fig. 11, deeper in the actinide region the discrepancies in the predictions of both models and of the different values of a_f/a_n disappear.

A small modification in ALICE-91 enables us to extract the contribution to the fission cross section from each evaporation residue in the calculation for ^{232}Th. Applying the criterion of Eq. (2) we can again determine the decomposition of the calculated total fission cross section into a purely symmetric and a mixed contribution. The calculation is performed with the RLDM for $a_f/a_n=1.00$, since this gives the best description of the experimental fission cross section of ^{232}Th. The values for the calculated purely symmetric and the mixed fission cross section are added to Table IV and very close to the LAHET results. The experimental mixed fission cross section is lower than the calculated values, of both LAHET and ALICE-91, by approximately 30%.

VII. SUMMARY AND CONCLUSIONS

We have measured independent and cumulative fission-product yields originating from 190 MeV proton-induced reactions on ^{nat}W, ^{197}Au, ^{nat}Pb, ^{208}Pb, and ^{232}Th. With the experimental setups for the short irradiation (catcher cylinder) and the long irradiation (catcher foil) it is possible to observe both short-lived and long-lived fission products. We are able to distinguish between fission products leaving the target in forward and backward direction, but do not find any indication for the existence of an anisotropy in the angular distribution of the fission fragments.

The mass yields of ^{nat}W, ^{197}Au, and ^{208}Pb are well described by a single Gaussian both for the mass and the charge distribution. The mass yields of ^{nat}Pb agree within a factor of 2 with the single-Gaussian fit of the mass and charge distribution. The relative widths of the mass distributions are decreasing while going to higher fissility parameters. Fission cross sections extracted from the single-Gaussian fits are comparable with the values obtained from the fits of Eismont *et al.*

The fission cross section resulting from the single-Gaussian description for ^{232}Th underestimates the value of Eismont *et al.* by a factor of 2. Looking carefully at the mass yields for ^{232}Th, it is obvious that the mass yield curve has a more complicated form than that of a single Gaussian. The dip in the mass yield curve around mass 125 must represent a real feature of the true mass yield curve. We believe that the origin of this particular form of the mass distribution can be found in the process of multichance fission. Particle evaporation prior to fission results in a wide variety of fissioning nuclides, each contributing to the mass distribution with its own fission characteristics. In our view the observed strong symmetric component in the ^{232}Th mass distribution, at the high excitation energies encountered in this experiment, is only partly caused by an enhanced crossing of the symmetric fission barrier in the fissioning nuclides, which possess both symmetric and asymmetric fission modes. The largest contribution comes from purely symmetric fission in the neutron-poor region. We decompose the measured mass yield curve into a single Gaussian belonging to the purely symmetric fission mode and a contribution of three Gaussians, together describing mixed fission. The fission cross section resulting from this decomposition is slightly smaller than the value of Eismont *et al.*

Fission cross sections and mass yield curves are calculated with the intranuclear cascade code LAHET employing the RAL model by Atchison for fission. The mass yield curve for ^{232}Th lacks the purely symmetric contribution, but the fission cross section agrees very well with our value from the decomposition of the ^{232}Th mass distribution. LAHET underpredicts the fission cross section for the subactinides ^{nat}W and ^{208}Pb severely and overestimates in general the width of the mass distribution.

Fission cross sections are also computed with the ALICE-91 code. The rotating finite-range model by Sierk gives a better prediction of the experimental data for the subactinides than the rotating-liquid-drop model. A somewhat larger value for the ratio of the fission saddle-point to the ground-state level densities is needed to obtain agreement for the lighter targets in comparison to the heavier targets. Fission of ^{232}Th is best described by the rotating-liquid-drop model.

LAHET and ALICE-91 calculations reproduce the experimental values of the purely symmetric and the mixed fission cross section of ^{232}Th surprisingly well, despite the rather *ad hoc* assumption of four Gaussians describing the mass distribution and only one Gaussian representing the charge distribution. The mixed fission cross section is in both calculations 30% higher than the experimentally determined value, while the experimental and calculated cross section for purely symmetric fission agree within uncertainty limits with each other. This is very encouraging for our assumption that a distinction between mixed and symmetric fissioning nuclides can be made, based on a *Z*-dependent criterion on the fissility parameter.

This work has been supported by the ''Stichting voor Fundamenteel Onderzoek der Materie'' (FOM) with financial support from the ''Nederlandse Organisatie voor Wetenschappelijk Onderzoek'' (NWO).

[1] C. Wagemans, *The Nuclear Fission Process* (CRC Press, Boca Raton, 1991).
[2] L. Nikkinen, B. P. Pathak, L. Lessard, and I. S. Grant, Phys. Rev. C **22**, 617 (1980).
[3] R. Holub and L. Yaffe, J. Inorg. Nucl. Chem. **35**, 3991 (1973).
[4] J. F. Croall and J. G. Cuninghame, Nucl. Phys. **A125**, 402 (1969).
[5] B. L. Tracy, J. Chaumont, R. Klapisch, J. M. Nitschke, A. M. Poskanzer, E. Roeckl, and C. Thibault, Phys. Rev. C **5**, 222 (1972).
[6] T. McGee, C. L. Rao, and L. Yaffe, Nucl. Phys. **A173**, 595 (1971).
[7] M. Lindner and R. N. Osborne, Phys. Rev. **94**, 1323 (1954).
[8] X. Blanchard, J. L. Flament, J. Fréhaut, J. Laurec, P. Morel, B. Cordier, N. Diallo, and F. Albernhe, in Proceedings of the Second International Conference on Accelerator Driven Transmutation Technologies and Applications, Kalmar, Sweden, 1996, edited by H. Condé (Uppsala University), Vol. I, p. 543.
[9] V. S. Bychenkov, M. F. Lomanov, A. I. Obukhov, N. A. Perfilov, O. E. Shigaev, G. G. Shimchuk, and R. M. Yakovlev, Sov. J. Nucl. Phys. **17**, 496 (1973).
[10] J. A. Panontin and N. T. Porile, J. Inorg. Nucl. Chem. **30**, 2891 (1968).
[11] Y. V. Alexandrov, V. P. Eismont, R. B. Ivanov, M. A. Mikhailova, V. P. Prikhodtseva, A. V. Saulsky, and S. K. Vasiljev, in Proceedings of the Second International Conference on Accelerator Driven Transmutation Technologies and Applications [8], Vol. II, p. 576.
[12] E. Hagebø and T. Lund, J. Inorg. Nucl. Chem. **37**, 1569 (1975).
[13] M. Gloris, R. Michel, U. Herpers, F. Sudbrock, and D. Filges, Nucl. Instrum. Methods Phys. Res. B **113**, 429 (1996).
[14] R. Michel, R. Bodemann, H. Busemann, R. Daunke, M. Gloris, H.-J. Lange, B. Klug, A. Krins, I. Leya, M. Lüpke, S.

Neumann, H. Reinhardt, M. Schnatz-Büttgen, U. Herpers, Th. Schiekel, F. Sudbrock, B. Holmqvist, H. Condé, P. Malmborg, M. Sutter, B. Dittrich-Hannen, P.-W. Kubik, H.-A. Synal, and D. Filges, Nucl. Instrum. Methods Phys. Res. B **129**, 153 (1997).

[15] E. Gadioli and P. E. Hodgson, *Pre-equilibrium Reactions* (Clarendon, Oxford, 1992).

[16] M. Blann, presented at the Workshop on Computation and Analysis of Nuclear Data Relevant to Nuclear Energy and Safety, Trieste, Italy, 1992; LLNL Report No. UCRL-JC-109052, 1991.

[17] R. E. Prael and H. Lichtenstein, ''User Guide to LCS: The LAHET Code System,'' Report No. LA-UR-89-3014, Los Alamos National Laboratory, 1989.

[18] Evaluated Nuclear Structure Data File (ENSDF), produced by members of the International Nuclear Structure and Decay Data Network, and maintained by the National Nuclear Data Center, BNL.

[19] G. F. Steyn, S. J. Mills, F. M. Nortier, B. R. S. Simpson, and B. R. Meyer, Appl. Radiat. Isot. **41**, 315 (1990).

[20] J. F. Ziegler, J. P. Biersack, and U. Littmark, *The Stopping and Range of Ions in Solids* (Pergamon Press, New York, 1985).

[21] V. E. Viola, K. Kwiatkowski, and M. Walker, Phys. Rev. C **31**, 1550 (1985).

[22] V. S. Bychenkov, V. D. Dmitriev, A. I. Obukhov, N. A. Perfilov, and O. E. Shigaev, Sov. J. Nucl. Phys. **30**, 16 (1979).

[23] Application Software Group, CERN Program Library, Q121, 1991.

[24] F. D. Becchetti, J. Jänecke, P. Lister, K. Kwiatowski, H. Karwowski, and S. Zhou, Phys. Rev. C **28**, 276 (1983); F. D. Becchetti, K. H. Hicks, C. A. Fields, R. J. Peterson, R. S. Raymond, R. A. Ristinen, J. L. Ullmann, and C. S. Zaidins, *ibid.* **28**, 1217 (1983).

[25] V. P. Eismont, A. I. Obukhov, A. V. Prokofyev, and A. N. Smirnov, in Proceedings of the Second International Conference on Accelerator Driven Transmutation Technologies and Applications [8], Vol. II, p. 592.

[26] C. Chung and J. J. Hogan, Phys. Rev. C **24**, 180 (1981).

[27] C. Chung and J. J. Hogan, Phys. Rev. C **25**, 899 (1982).

[28] H. Kudo, H. Muramatsu, and H. Nakahara, Phys. Rev. C **25**, 3011 (1982).

[29] K.-H. Schmidt, A. Heinz, H.-G. Clerc, B. Blank, T. Brohm, S. Czajkowski, C. Donzaud, H. Geissel, E. Hanelt, H. Irnich, M. C. Itkis, M. de Jong, A. Junghans, A. Magel, G. Münzenberg, F. Nickel, M. Pfützner, A. Piechaczek, C. Röhl, C. Scheidenberger, W. Schwab, S. Steinhäuser, K. Sümmerer, W. Trinder, B. Voss, and S. V. Zhdanov, Phys. Lett. B **325**, 313 (1994).

[30] A. C. Pappas and E. Hagebø; J. Inorg. Nucl. Chem. **28**, 1769 (1966).

[31] C. H. Lee, Y. W. Yu, D. Lee, H. Kudo, K. J. Moody, and G. T. Seaborg, Phys. Rev. C **38**, 1757 (1988).

[32] A. S. Jensen and J. Damgaard, Nucl. Phys. **A203**, 578 (1973).

[33] F. Atchison, in ''Targets for Neutron Beam Spallation Sources,'' Report No. Jül-Conf-34, Kernforschungsanlage Jülich GmbH, Germany, 1980.

[34] A. J. Sierk, Phys. Rev. C **33**, 2039 (1986).